Analog Gated Recurrent Unit Neural Network for Detecting Chewing Events

Kofi Odame , Senior Member, IEEE, Maria Nyamukuru, Student Member, IEEE, Mohsen Shahghasemi, Student Member, IEEE, Shengjie Bi, and David Kotz, Fellow, IEEE

Abstract—We present a novel gated recurrent neural network to detect when a person is chewing on food. We implemented the neural network as a custom analog integrated circuit in a 0.18 μm CMOS technology. The neural network was trained on 6.4 hours of data collected from a contact microphone that was mounted on volunteers' mastoid bones. When tested on 1.6 hours of previously-unseen data, the analog neural network identified chewing events at a 24-second time resolution. It achieved a recall of 91% and an F1-score of 94% while consuming 1.1 μW of power. A system for detecting whole eating episodes—like meals and snacks—that is based on the novel analog neural network consumes an estimated 18.8 μW of power.

Index Terms—Analog LSTM, eating detection, neural networks, wearable devices.

I. INTRODUCTION

ONITORING food intake and eating habits are important for managing and understanding obesity, diabetes and eating disorders [1], [2], [3]. Because self-reporting is unreliable, many wearable devices have been proposed to automatically monitor and record individuals' dietary habits [4], [5], [6], [7]. The challenge is that these devices store or transmit raw data for offline processing. This is a power-consumptive approach that requires a bulky battery or frequent charging, which intrudes on the user's normal daily activities and is thus prone to poor user adherence and acceptance [8], [9], [10], [11].

We recently addressed this problem with a long short-term memory (LSTM) neural network for eating detection that can

Manuscript received 24 July 2022; revised 12 September 2022 and 21 October 2022; accepted 23 October 2022. Date of publication 2 November 2022; date of current version 14 February 2023. This work was supported by the U.S. National Science Foundation under Grants CNS-1565269 and CNS-1835983. This paper was recommended by Associate Editor A. Basu. (Corresponding author: Kofi Odame.)

Kofi Odame, Maria Nyamukuru, and David Kotz are with Dartmouth College, Hanover, NH 03755 USA (e-mail: kofi.m.odame@dartmouth.edu; maria.t.nyamukuru.th@dartmouth.edu; david.f.kotz@dartmouth.edu).

Mohsen Shahghasemi was with Dartmouth College, Hanover, NH 03755 USA. He is now with Apple Inc., Cupertino, CA 95014 USA (e-mail: mohsen.shahghasemi.th@dartmouth.edu).

Shengjie Bi was with Dartmouth College, Hanover, NH 03755 USA. He is now with Meta Platforms Inc., Menlo Park, CA 94025 USA (e-mail: shengjie.bi@dartmouth.edu).

This work involved human subjects or animals in its research. Approval of all ethical and experimental procedures and protocols was granted by the Dartmouth College Institutional Review Board (Committee for the Protection of Human Subjects-Dartmouth; Protocol Number: 00030005) in accordance with U.S. Department of Health and Human Services regulation 45 CFR 46.

Color versions of one or more figures in this article are available at https://doi.org/10.1109/TBCAS.2022.3218889.

Digital Object Identifier 10.1109/TBCAS.2022.3218889

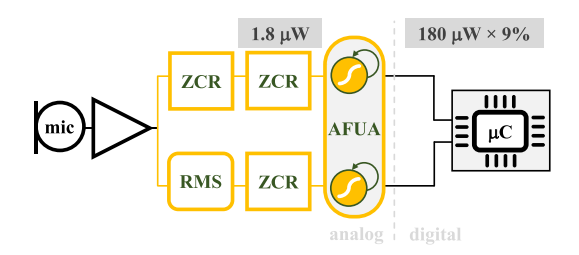


Fig. 1. Block diagram of proposed eating detection system. From the contact microphone output, the ZCR and RMS blocks extract features based on zero-crossing rate and root-mean-square. The analog neural network (labelled 'AFUA') processes these features and produces a one-hot encoded output that predicts the presence or absence of a chewing event. The microcontroller (' μ C') merges and filters the individual chewing events into whole eating episodes. The analog signal processing chain up to the AFUA block consumes 1.8 μ W of power. The microcontroller is active only 9 % of the time, during which it consumes 180 μ W of power.

be embedded on the wearable device [12], [13]. However, that approach required a power-consumptive analog-to-digital converter (ADC). It also required the microcontroller unit (MCU) to unnecessarily spend power processing irrelevant data.

Analog LSTM neural networks have been proposed as a way to eliminate the ADC and also to minimize the microcontroller's processing of irrelevant data. Unfortunately, the state-of-the-art analog LSTMs [14], [15], [16], [17], [18] are implemented with operational amplifiers (opamps), current/voltage converters, Hadamard multiplications and internal ADCs and digital-to-analog converters (DACs). These peripheral components represent a significant amount of overhead cost in terms of power consumption, which diminishes the benefits of an analog LSTM (see Table I).

In this paper, we present the design, implementation, analysis and measurement results of a novel analog integrated circuit LSTM for embedded eating event detection that eliminates the need for a power-consumptive ADC. Unlike previous analog LSTM implementations, our solution contains no internal DACs, ADCs, opamps or Hadamard multiplications. Our novel approach is based on a current-mode adaptive filter, and it eliminates over 90% of the power requirements of a more conventional solution.

II. EATING DETECTION SYSTEM

Fig. 1 shows our proposed Adaptive Filter Unit for Analog (AFUA) long short-term memory as part of a signal processing system for detecting eating episodes. The input to the system

1932-4545 © 2022 IEEE. Personal use is permitted, but republication/redistribution requires IEEE permission. See https://www.ieee.org/publications/rights/index.html for more information.

TABLE I

THE PROPOSED LSTM ('AFUA') HAS THE FEWEST PERIPHERAL COMPONENTS AND HENCE THE LOWEST POWER CONSUMPTION OVERHEAD (SEE SECTION IV-A DERIVATION). m AND n ARE Number of Hidden States and Inputs, Respectively

Architecture	LSTM Type	$m \times n$	Power Consumption Overhead (%)				
			ADC	DAC	Buffer	Opamp, V/I	Total
This work	AFUA	10×16	0	0	3	0	3
[19]	GRU	10×16	0	0	32	0	32
[17]	Classical LSTM	128×128	12	25	1	30	68
[18]	Classical LSTM	16×16	3	17	8	1	29

Note: For a given analog LSTM architecture, the larger the $m \times n$ product, the smaller the overhead. For fair comparison, we report AFUA overhead cost for $m \times n = 10 \times 16$. The core processing block for all the LSTM architectures is based on the same basic vector matrix multiplier (VMM) structure. If we implement each architecture in the same process technology node with the same VMM, then the architecture with the least overhead will consume the least total power.

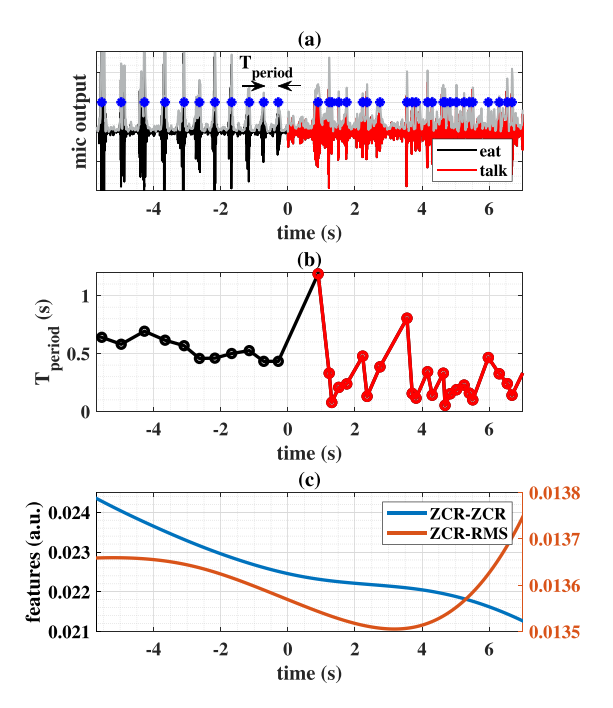


Fig. 2. Typical time series data for chewing and talking events. (a) Data from contact microphone shows that chewing (time $<0~\rm s$) is characterized by quasiperiodic bursts. No quasi-periodicity is observed during talking (time $\geq0~\rm s$). (b) Duration between signal bursts ('T $_{\rm period}$ '). For the chewing event (time $<0~\rm s$), $T_{\rm period}$ is relatively constant. In contrast, $T_{\rm period}$ varies widely during the talking event. (c) Features extracted from microphone output.

is produced by a contact microphone that is mounted on the user's mastoid bone. Features are extracted from the contact microphone signal and input to the AFUA neural network, which infers whether or not the user is chewing. The AFUA's output is a one-hot encoding ((2,0)= chewing; (0,2)= not chewing) of the predicted class label. Finally, a microcontroller processes the predicted class labels and groups the chewing events into discrete eating episodes, like a meal, or a snack [4], [5]. Following is a detailed description of the feature extraction and neural network components of the system.

A. Feature Extraction

As demonstrated in Fig. 2, chewing is characterized by quasiperiodic bursts of large amplitude, low frequency signals that can be measured by a contact microphone or accelerometer that is mounted on the head [5], [12]. We can use the root mean square (RMS) and the zero-crossing rate (ZCR) to capture the signal's amplitude and frequency, respectively. A second ZCR operation applied to the RMS and the initial ZCR will produce information about the signal's periodicity. The RMS block is simply an envelope detector [20]. The ZCR block comprises a zero-crossing detector [21] followed by a bandlimited transconductance amplifier that integrates the detected zero crossings over time.

B. Analog LSTM

Fundamentally, an LSTM is a neuron that selectively retains, updates or erases its memory of input data [22]. The gated recurrent unit (GRU) is a simplified version of the classical LSTM, and it is described with the following set of equations [23]:

$$r_{i} = \sigma([\mathbf{W}_{r}\mathbf{x}]_{i} + [\mathbf{U}_{r}\mathbf{h}_{\langle t-1\rangle}]_{i}) \tag{1}$$

$$z_j = \sigma([\mathbf{W}_z \mathbf{x}]_j + [\mathbf{U}_z \mathbf{h}_{\langle t-1 \rangle}]_j)$$
 (2)

$$\tilde{h}_{j}^{\langle t \rangle} = \tanh([\mathbf{W}\mathbf{x}]_{j} + [\mathbf{U}(\mathbf{r} \odot \mathbf{h}_{\langle t-1 \rangle})]_{j})$$
(3)

$$h_j^{\langle t \rangle} = z_j h_j^{\langle t-1 \rangle} + (1 - z_j) \tilde{h}_j^{\langle t \rangle}, \tag{4}$$

where \mathbf{x} is the input, h_j is the hidden state, \tilde{h}_j is the candidate state, r_j is the reset gate and z_j is the update gate. Also, \mathbf{W}_* and \mathbf{U}_* are learnable weight matrices.

To implement the GRU in an efficient analog integrated circuit that contains no DACs, ADCs, operational amplifiers or multipliers, we can transform (1)-(4) as follows. The σ function of (2) gives z_j a range of (0,1), and the extrema of this range reveals the basic mechanism of the update equation, (4). For $z_j=0$, the update equation is $h_j^{\langle t \rangle}=\tilde{h}_j^{\langle t \rangle}$. For $z_j=1$, the update equation becomes $h_j^{\langle t \rangle}=h_j^{\langle t-1 \rangle}$. Without loss of generality, we can replace $(1-z_j)$ with z_j (this merely inverts the logic of the update gate, and inverts the sign of the \mathbf{W}_z and \mathbf{U}_z weight matrices). So, replacing $(1-z_j)$ and rearranging the update equation gives us

$$\left(h_{j}^{\langle t\rangle}-h_{j}^{\langle t-1\rangle}\right)/z_{j}+h_{j}^{\langle t-1\rangle}=\tilde{h}_{j}^{\langle t\rangle},\tag{5}$$

which is simply a first-order low pass filter with a continuoustime form of

$$\frac{\tau}{z_j(t)}\frac{dh_j}{dt} + h_j(t) = \tilde{h}_j(t),\tag{6}$$

where $\tau = \Delta T$, the time step of the discrete-time system. The gating mechanics of the continuous- versus discrete-time update equations are equivalent, modulo the inverted logic: For $z_i(t) =$

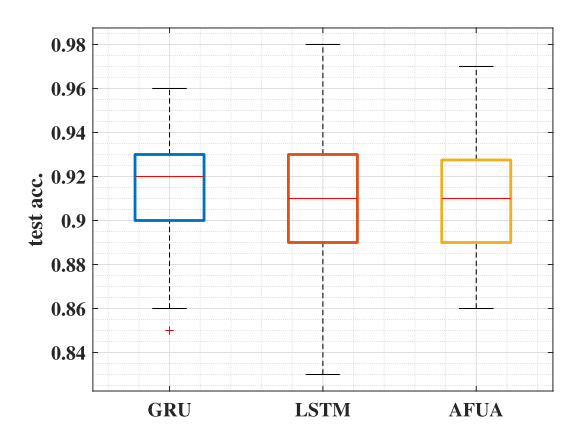


Fig. 3. Simulation results (test set accuracy) for 10-class keyword spotting task [28], [29]. The simulated neural network architecture comprises: a 16-unit LSTM input layer, a second 16-unit LSTM layer, a 10-unit dense layer (ReLU activations) and a 10-unit dense output layer (softmax activations). We implemented the LSTM layers first with GRU [23], then classical LSTM [22] and finally AFUA neurons.

0, (6) is a low-pass filter with an infinitely large time constant, and $h_j(t)$ does not change (this is equivalent to $h_j^{\langle t \rangle} = h_j^{\langle t-1 \rangle}$ in discrete time). For $z_j(t)=1$, (6) is a low-pass filter with a time constant of $\tau=\Delta T$. Since the ΔT time step is small relative to the GRU's dynamics, a time constant of $\tau=\Delta T$ produces $h_j(t)\approx \tilde{h}_j(t)$ (equivalent to $h_j^{\langle t \rangle}=\tilde{h}_j^{\langle t \rangle}$ in discrete time).

Various studies [13], [24], [25], [26] have found the reset gate unnecessary with slow-changing signals, and for event detection. As these scenarios describe our eating detection application, we can discard the reset gate.

Finally, if we translate the origins [27] of both $h_j(t)$ and $\tilde{h}_j(t)$, then we can replace the tanh with a saturating function that has a range of (0,1). Such a saturating function can easily be implemented in analog circuitry, by taking advantage of the unidirectional nature of a transistor's drain-source current. We replace both the tanh and the σ with the following saturating function,

$$f(y) = \frac{\max(y,0)^2}{1 + \max(y,0)^2},\tag{7}$$

translate the origin and discard the reset gate to arrive at the *Adaptive Filter Unit for Analog LSTM* (AFUA):

$$z_j = f([\mathbf{W_z}\mathbf{x}]_j + [\mathbf{U_z}(\mathbf{h} - \mathbf{1}) + \mathbf{b_z}]_j)$$
 (8)

$$\tilde{h}_j = f([\mathbf{W}\mathbf{x}]_j + [\mathbf{U}(\mathbf{h} - \mathbf{1}) + \mathbf{b}]_j)$$
(9)

$$\frac{\tau}{z_j}\frac{dh_j}{dt} = 2\tilde{h}_j - h_j,\tag{10}$$

where $[\cdot]_j$ is the j'th element of the vector. Also, \mathbf{x} is the input, h_j is the hidden state and \tilde{h}_j is the candidate state. The variable τ is the nominal time constant, while z_j controls the state update rate in (10). $\mathbf{W}_{\mathbf{z}}$, $\mathbf{U}_{\mathbf{z}}$, \mathbf{W} , \mathbf{U} are learnable weight matrices, while $\mathbf{b}_{\mathbf{z}}$, \mathbf{b} are learnable bias vectors. Simulation results (Fig. 3) for a multi-class machine learning task show that the AFUA performs with a comparable level of accuracy as the GRU and classical LSTM.

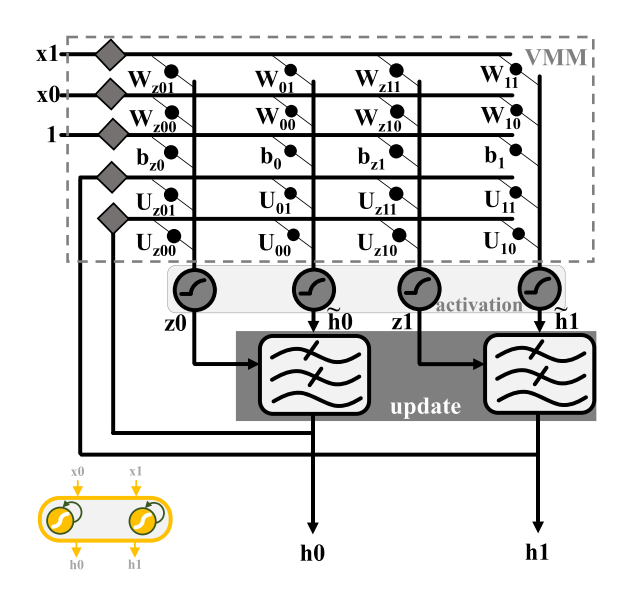


Fig. 4. High level architecture of the AFUA neural network, which has a two-dimensional input feature vector, $\mathbf{x} = [x_0, x_1]^{\mathrm{T}}$. The network keeps a memory of past inputs by feeding back its hidden states, h_0, h_1 , to the vector matrix multiplier (VMM). The persistence of the network's memory depends on the time constants, z_0, z_1 , of the adaptive low pass filters in the 'update' block. Finally, the 'activation' block provides saturating nonlinearities described by (7).

III. ANALOG LSTM CIRCUIT IMPLEMENTATION

Fig. 4 shows the high-level block diagram of the AFUA neural network. It comprises two AFUA cells (with corresponding hidden states h_0 and h_1), and it accepts two inputs, x_0 and x_1 . Unlike previous LSTMs [14], [15], [16], [17], [18], the AFUA network contains no digital-to-analog converters, analog-to-digital converters, operational amplifiers or four-quadrant multipliers. Avoiding these power-consumptive components is what makes the AFUA implementation so efficient. Following are the circuit implementation details of the AFUA.

A. Dimensionalization

To realize the AFUA (8), (9), (10) and (7) as an analog circuit, we first 'dimensionalize' each variable and implement it as the ratio of a time-varying current and a fixed unit current, $I_{\rm unit}$ [30], [31]. For instance, we represent the update gate variable, z_j , as $I_z/I_{\rm unit}$.

B. Activation Function

The (7) function is implemented as the current-starved current mirror shown in Fig. 5. Kirchhoff's Current Law applied to the source of transistor M_3 gives

$$I_{\text{out}} = I_3 = I_{\text{unit}} - I_4.$$
 (11)

The transistors are all sized equally, meaning that, from Kirchhoff's Voltage Law, the gate source voltage of transistor M_3 is

$$V_{\text{GS3}} = 2V_{\text{GS1}} + V_{\text{GS4}} - 2V_{\text{GSa}},$$
 (12)

where we have assumed that the body effect in M_2 and M_b is negligible. If we operate the transistors in the subthreshold

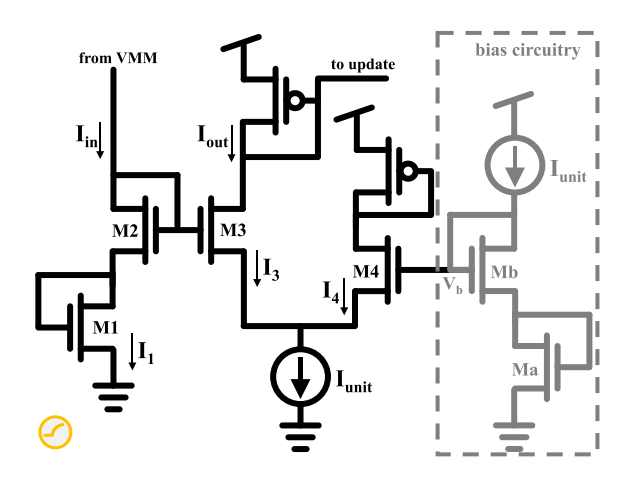


Fig. 5. Activation function circuit schematic. A version of the input signal, $I_{\rm in}$, is reflected as current $I_{\rm out}$. The tail bias current source of the M₃-M₄ differential pair limits the output current to $I_{\rm out} < I_{\rm unit}$. Also, the one-sidedness of the nMOS drain current limits $I_{\rm out}$ to positive values only. In summary, the activation function circuit produces $0~{\rm A} \le I_{\rm out} < I_{\rm unit}$.

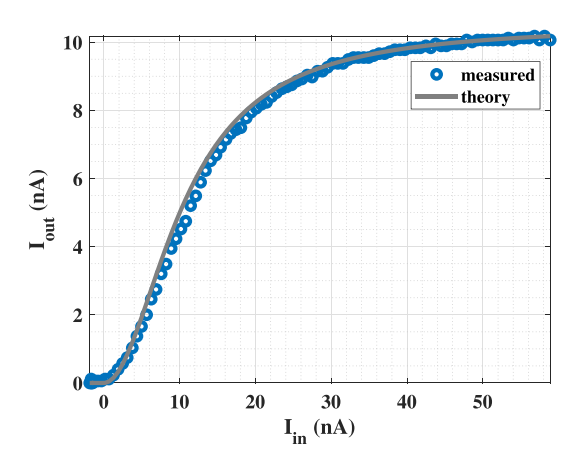


Fig. 6. Activation function transfer curve. Chip measurements of the Fig. 5 circuit closely match the theoretically-predicted behavior of (15) for $I_{\rm unit}=10.5\,{\rm nA}.$ The saturating behavior is analogous to that of the original GRU's sigmoid.

region, then (12) implies

$$I_{\text{out}} = I_3 = \frac{I_4 I_1^2}{I_{\text{unit}}^2}.$$
 (13)

Combining (11) and (13) gives us

$$I_{\text{out}} = \frac{I_{\text{unit}} I_1^2}{I_{\text{unit}}^2 + I_1^2}.$$
 (14)

Now, the current flowing through a diode-connected nMOS is unidirectional, meaning $I_1 = \max(I_{\rm in}, 0)$, and we can write

$$I_{\text{out}} = I_{\text{unit}} \cdot \frac{\max(I_{\text{in}}, 0)^2}{I_{\text{unit}}^2 + \max(I_{\text{in}}, 0)^2},$$
 (15)

which is a dimensionalized analog of (7). The measurement results in Fig. 6 illustrate the nonlinear, saturating behavior of this activation function.

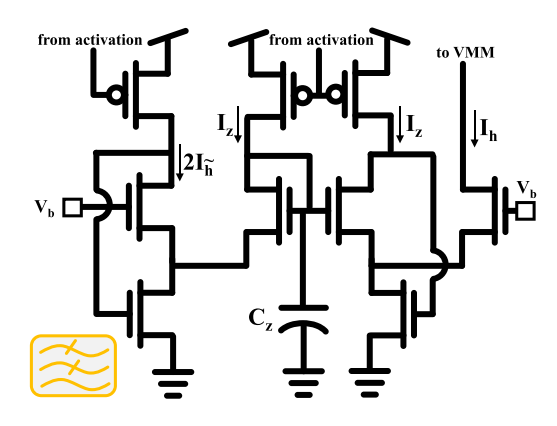


Fig. 7. State update circuit schematic. The output I_h is a low-pass-filtered version of the input, $2I_{\tilde{h}}$. The filter's time constant is inversely proportional to the value of the current I_z . So, large values of I_z increase the rate at which I_h updates to $2I_{\tilde{h}}$, while small values of I_z slow down this process.

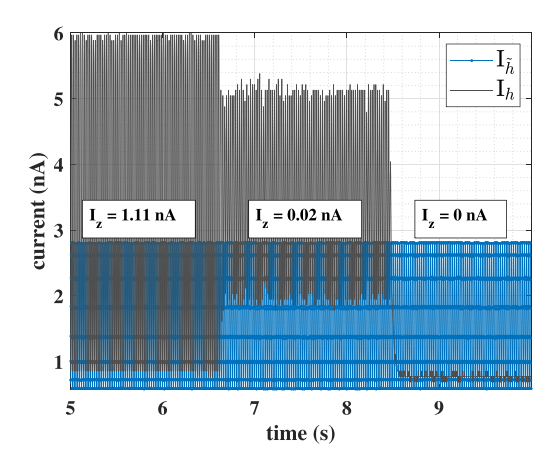


Fig. 8. State update circuit response. Chip measurements of the Fig. 7 circuit show that the output, I_h follows the input, $I_{\tilde{h}}$ at a rate that is determined by the value of current I_z .

C. State Update

The AFUA state update, (10), is implemented as the adaptive filter shown in Fig. 7. The currents I_h , $I_{\tilde{h}}$ and I_z represent the hidden state h_j , the candidate state \tilde{h}_j and the update gate, z_j , respectively. From the translinear loop principle, the Fig. 7 circuit's dynamics can be written as [30], [32]

$$\underbrace{\frac{C_z U_{\rm T}}{\kappa I_{\rm unit}}}_{I_z} \frac{I_{\rm unit}}{I_z} \frac{dI_h}{dt} = 2I_{\tilde{h}} - I_h, \tag{16}$$

where κ is the body-effect coefficient and $U_{\rm T}$ is the thermal voltage [33]. Just as z_j does for h_j in (10), I_z controls the update speed of I_h (see Fig. 8).

D. Vector Matrix Multiplication

Fig. 9 depicts the components of our vector-matrix multiplication (VMM) block. These are the soma and synapse circuits that are common in the analog neuromorphic literature [34]. Crucially, the soma-synapse architecture is current-in, current-out. This means that, unlike other approaches for implementing GRU and LSTM networks [15], [16], [17], the VMM does

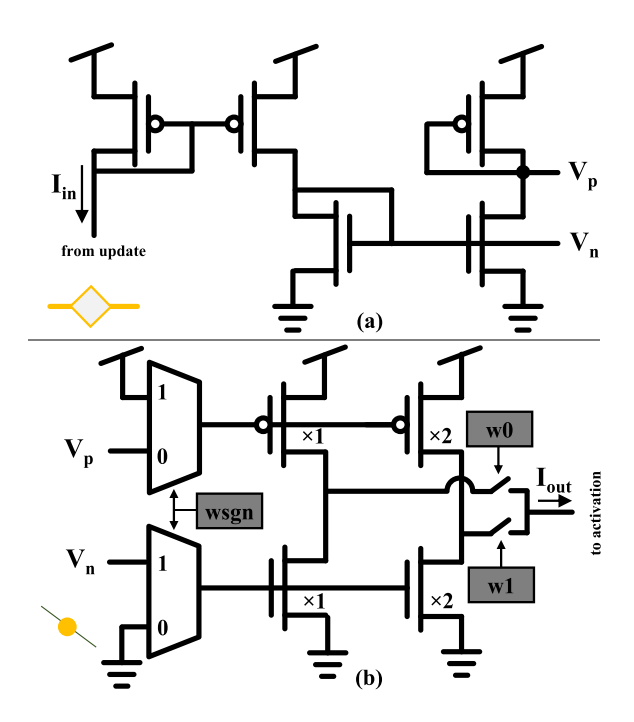


Fig. 9. Vector matrix multiplier circuit components. (a) The soma is as a current-mode buffer. (b) The synapse is a programmable current mirror, with gain stored in registers $w_{\rm sgn}$, w_0 , w_1 . These represent the neural network's 3-bit quantized learned weights.

not need power-consumptive operational amplifiers to convert signals between the current and voltage domains.

IV. ANALOG LSTM CIRCUIT ANALYSIS

The following subsections address various practical aspects of an actual AFUA implementation.

A. Current Consumption

Since the activation function, (7), has a range of (0,1), the z_j and \tilde{h}_j variables are likewise limited to (0,1). Also, from (10), h_j spans (0,2). This means that all update gate and candidate state currents have a maximum value of I_{unit} , while the hidden state currents have a maximum value of $2I_{\text{unit}}$. With this information, we can calculate upper-bounds on the current consumption of each circuit component.

- 1) Activation Function: Not counting the input current that is supplied by the VMM, Fig. 5 shows that the only current consumed by the activation function block is the differential-pair tail current of $I_{\rm unit}$. There are two activation functions per AFUA cell (one each for z_j and \tilde{h}_j). So, for an m-unit AFUA layer, the activation function blocks draw a total current of $m \times 2I_{\rm unit}$.
- 2) State Update: The total current flowing through the four branches of the state update circuit (Fig. 7) is $2\tilde{I}_h + 2I_z + I_h$, which has a worst-case value of $6I_{\rm unit}$. For our m-unit AFUA network, the state update circuits consume at most $m \times 6I_{\rm unit}$.
- 3) VMM Soma: The soma is a current-mode buffer that drives a differential signal onto each row of the VMM (see Fig. 9). For the somas on the input and bias rows, the maximum current consumption is $2I_{\rm unit}$. The somas driving the hidden state rows consume at most $4I_{\rm unit}$ each. So, with n inputs, m hidden states

and one bias row, the somas will consume a maximum total current of $(n+2m+1)\times 2I_{\rm unit}$.

- 4) VMM Core: As depicted in Fig. 9, each multiplier element in the VMM core comprises a number of current sources that are switched on or off, depending on the values of the weight bits $(w_{\rm sgn},\,w_0,\,w_1)$. At worst, all current sources are switched on, in which case the VMM elements that process state variables each consume $6I_{\rm unit}$, while those that process input variables or biases each consume $3I_{\rm unit}$. The maximum current draw of each VMM column for an n-input AFUA layer with m hidden states is therefore $(n+2\,m+1)\times 3I_{\rm unit}$. There are $2\,m$ columns, to give a total maximum VMM core current consumption of $m(n+2\,m+1)\times 6I_{\rm unit}$.
- 5) Total Current Consumption: From the previous subsections, we conclude that the worst-case total current consumption of an n-input AFUA layer with m hidden states is

$$I_{\text{tot}} \le (\underbrace{m(14 + 6(n+2m))}_{\text{core}} + \underbrace{4m + 2n + 2}_{\text{VMM soma}}) \times I_{\text{unit}}, \quad (17)$$

where 'core' includes the activation function, VMM core and state update current consumption. The VMM soma is peripheral to the AFUA's operation and represents overhead cost. For instance, a 16-input, 10-unit AFUA layer would spend 3% of its power budget as overhead.

Empirically, we found that the average current consumption of some of the AFUA blocks is significantly lower than their estimated worst-case values. In particular, the VMM consumes only $48I_{\rm unit}$ on average. This leads to an average AFUA total current consumption of $62I_{\rm unit}$. The specific choice of $I_{\rm unit}$ depends on the desired operating speed, as we discuss in the following subsection.

B. Estimated Power Efficiency

The power efficiency of neural networks is conventionally measured in operations per Watt. But this metric does not apply directly to a system like the AFUA, since it executes all of its operations continuously and simultaneously. However, we can estimate the AFUA's power efficiency by considering the performance of an equivalent discrete time system.

To arrive at the discrete-form AFUA unit, we first replace the state variables of (8), (9) and (10) with their discrete-time counterparts. This includes the discretization $dh_j/dt = (h_j^{\langle t \rangle} - h_j^{\langle t-1 \rangle})/\Delta T$, where ΔT is the sampling period. Then, we set $\tau = \Delta T$ to produce the following expression.

$$z_{j} = f([\mathbf{W}_{\mathbf{z}}\mathbf{x}]_{j} + [\mathbf{U}_{\mathbf{z}}(\mathbf{h} - \mathbf{1}) + \mathbf{b}_{\mathbf{z}}]_{j})$$

$$\tilde{h}_{j}^{\langle t \rangle} = f([\mathbf{W}\mathbf{x}]_{j} + [\mathbf{U}(\mathbf{h}_{\langle t-1 \rangle} - \mathbf{1}) + \mathbf{b}]_{j})$$

$$h_{j}^{\langle t \rangle} = z_{j}2\tilde{h}_{j}^{\langle t \rangle} - (1 - z_{j})h_{j}^{\langle t-1 \rangle}.$$
(18)

For our application, \mathbf{W} , $\mathbf{W}_{\mathbf{z}}$ are 2×2 matrices, \mathbf{U} , $\mathbf{U}_{\mathbf{z}}$ are 1×2 vectors and z_j are scalars. So, each discretized AFUA unit executes 14 multiply operations per time step. Also, there are 2 divisions due to the two activation functions (see (7)). Not counting additions and subtractions, each discretized AFUA unit executes 16 operations per time step, to make for a total

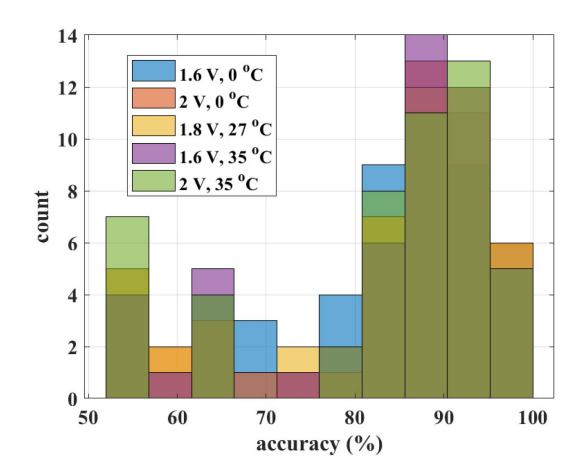


Fig. 10. Monte Carlo analysis performed for 250 runs, including mismatch and process variation, as well as power supply voltage and temperature corners of $\{1.6\,V,2V\}$ and $\{0\,^{\circ}\mathrm{C},35\,^{\circ}\mathrm{C}\}$, respectively. Nominal power supply voltage and temperature are $1.8\,V,27\,^{\circ}\mathrm{C}$. Median accuracy is $90\,\%$.

of 32 operations/step performed by the network. Assuming the sampling period of $\Delta T = 2$ ms used in our previous eating detection systems [7], [12], this implies the AFUA performs the equivalent of 16,000 operations per second.

Now, setting $\tau = \Delta T = 2$ ms requires a unit current of

$$I_{\text{unit}} = \frac{C_{\text{z}}U_{\text{T}}}{\kappa \tau} = 500 \cdot \frac{C_{\text{z}}U_{\text{T}}}{\kappa},$$
 (19)

where $C_z=57$ fF is the integrating capacitor of the translinear loop filter, $U_{\rm T}=26$ mV at room temperature and $\kappa\approx0.42$. This gives $I_{\rm unit}=1.8$ pA. With a total current consumption of $62I_{\rm unit}$, a voltage supply of 1.8 V and 16 K operations per second, the AFUA's equivalent operations per Watt is 76 TOps/W.

C. Mismatch

Due to random variations in doping and geometry, transistors that are nominally identical will exhibit mismatch when fabricated in a physical ASIC. To understand the effect of mismatch and other non-idealities on the AFUA neural network's performance, we performed Monte Carlo analyses with foundry-provided manufacturing and test data. The Monte Carlo analyses included mismatch and process variation, as well as power supply voltage and temperature corners of $\{1.6\,V, 2V\}$ and $\{0\,^{\circ}\mathrm{C}, 35\,^{\circ}\mathrm{C}\}$, respectively.

Fig. 10 shows the variation in classification accuracy for 250 Monte Carlo runs of one implementation of the AFUA neural network. The median accuracy across all runs is 0.90. Most of the variation in accuracy is due to mismatch, and the AFUA neural network is largely robust to temperature, voltage and process variation. The neural network is also unaffected by circuit noise (this is a direct result of the network's ability to generalize). To mitigate the effect of mismatch, we can use larger transistors [35], calibrate the network's learning algorithm for each individual chip [34], or incorporate mismatch data into a fault-tolerant learning algorithm [36].



Fig. 11. Left panel: a contact microphone was used to collect acoustic data from the mastoid bone as study participants performed various eating and noneating tasks [6]. Right panel: prototype of the complete wearable device that we are developing for dietary monitoring [7].

V. EXPERIMENTAL METHODS

A. Data Collection

Training and testing data was collected from study volunteers in a laboratory setting. All aspects of the study protocol were reviewed and approved by the Dartmouth College Institutional Review Board (Committee for the Protection of Human Subjects-Dartmouth; Protocol Number: 00030005).

The data used for this study was previously collected in a controlled laboratory setting from 20 participants (8 females, 12 males; aged 21–30) that were instructed to perform both eating and non-eating-related activities. During these activities, a contact microphone (see Fig. 11) was secured behind the ear with a headband, to measure any acoustic signals present at the tip of the mastoid bone [6]. The output of the contact microphone was digitized and stored using a 20 kSa/s, 24-bit data acquisition device (DAQ).

Participants were asked to eat a variety of foods—including carrots, protein bars, crackers, canned fruit, instant food, and yogurt—for at least 2 minutes per food type. This resulted in a 4 h total eating dataset. Non-eating activities included talking and silence for 5 minutes each and then coughing, laughing, drinking water, sniffling, and deep breathing for 24 seconds each. This resulted in 4 hours total of non-eating data. Each activity occurred separately and was classified based on activity type as eating or non-eating.

We down-sampled the DAQ data to 500 Hz and applied a high pass filter with a 20 Hz cutoff frequency to attenuate noise. We segmented the positive class data (chewing), and negative class data (not chewing) into 24-second windows with no overlap. The positive and negative class data were labelled with the one-hot encoding (2,0) and (0,2), respectively. Finally, we extracted the ZCR-RMS and ZCR-ZCR features of the windows to produce 2-dimensional input vectors to be processed by the AFUA network.

B. Neural Network Training

For training, the AFUA neural network was implemented in Python, using a custom layer defined by the discretized system of (18). Chip-specific parameters were extracted for each neuron and incorporated into the custom layers. The AFUA network was trained and validated on the laboratory data (train/valid/test

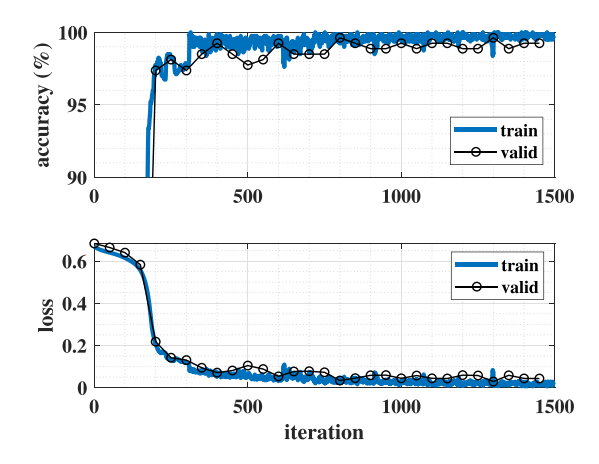


Fig. 12. Accuracy and loss training graphs for discretized AFUA neural network. We performed training in Python using the TensorFlow Keras v2.0 package. Validation set performance tracked that of the training set, indicating good generalization. The learned weights were quantized and programmed onto the AFUA ASIC's on-chip registers.

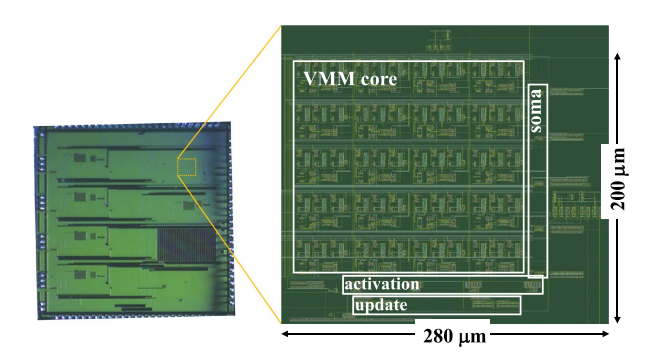


Fig. 13. Die photo of the AFUA ASIC, implemented in a $0.18\,\mu m$ CMOS process. The synapse circuits (labelled 'VMM core') consume most of the $200\,\mu m \times 280\,\mu$ m circuit area.

split: 68/12/20) using the TensorFlow Keras v2.0 package. Training was performed with the ADAM optimizer [37] and a weighted binary cross-entropy loss function to learn full-precision weights. Since the training data had a much higher sampling rate (500 Sa/s) than the bandwidth of the acoustic signals of interest (20 Hz), there was negligible information lost in the training process.

Python training was followed by a quantization step that converted the full-precision weights to signed 3-bit values $(0,\pm 1,\pm 2,\pm 3)$. An alternative approach would have been to directly incorporate the quantization process into the network's computational graph [13]. However, we found that such an approach only slows down training with no improvement in our network's classification performance.

C. Chip Measurements

The AFUA was implemented, fabricated and tested as an integrated circuit in a standard $0.18\,\mu\mathrm{m}$ mixed-signal CMOS process with a $1.8\,\mathrm{V}$ power supply. To simplify the measurement process and associated instrumentation, the ASIC I/O infrastructure includes current buffers that scale input currents by 1/100 and that multiply output currents by 100.

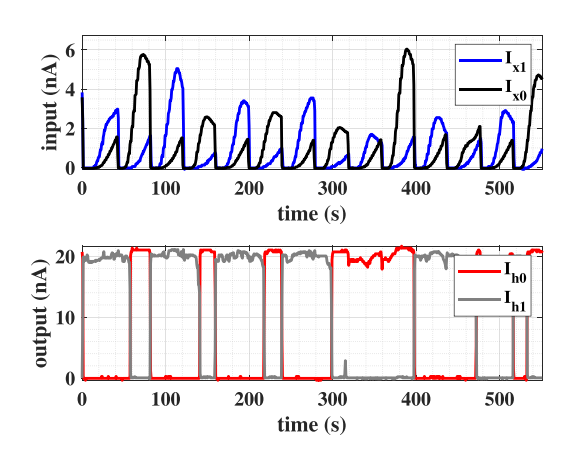


Fig. 14. AFUA chip measurement response to different input patterns (I_{x1},I_{x0}) taken from the test dataset. I_{x0} is the output of the cascade of an RMS block and ZCR block. I_{x1} is the output of the cascade of two ZCR blocks. The circuit's class prediction is encoded as output currents (I_{h1},I_{h0}) .

The AFUA neural network was programmed by storing the 3-bit version of each learned weight onto its corresponding onchip register in the VMM array.

The network was then evaluated on the test dataset. Specifically, each 24-second long window of 2-dimensional feature vectors from the test dataset was dimensionalized and scaled to $100 \times I_{\rm unit}$ and input to the ASIC with an arbitrary waveform generator. We set $I_{\rm unit} \approx 10$ nA with an off-chip resistor. According to (19), this $I_{\rm unit}$ creates a time constant of $\tau=0.36~\mu \rm s$, allowing for faster-than-real-time chip measurements—an important consideration, given the large amount of test data to be processed.

Output currents I_{h0} , I_{h1} were each measured from the voltage drop across an off-chip sense resistor. The ASIC's steady-state response was then taken as the classification decision. An output value of $(I_{h1}, I_{h0}) = (2I_{\rm unit}, 0)$ means that the circuit classified the input as eating, while $(I_{h1}, I_{h0}) = (0, 2I_{\rm unit})$ corresponds to non-eating. From these measurements, we calculated the algorithm's test accuracy, loss, precision, recall, and F1-score.

VI. RESULTS AND DISCUSSION

A. Classification Performance

Fig. 14 shows the AFUA chip's typical response to input data. The input currents I_{x1} , I_{x0} represent the ZCR-RMS and ZCR-ZCR features extracted from the contact microphone signal. Inputting a stream of I_{x1} , I_{x0} patterns produces output currents I_{h1} , I_{h0} , which represent the hidden states of the AFUA neural network.

According to our encoding scheme, $(I_{h1},I_{h0})=(2I_{\rm unit},0)$ means that the circuit classified the input as chewing, while $(I_{h1},I_{h0})=(0,2I_{\rm unit})$ corresponds to a prediction of not chewing. But the presence of noise and circuit non-ideality produces some ambiguity in the encoding: some AFUA output patterns can be interpreted as either chewing or not chewing, depending on the choice of threshold used to distinguish between 0 A and $2I_{\rm unit}$. Fig. 15 is the receiver operating characteristic curve (ROC) produced by varying this threshold current. The

TABLE II

COMPARISON BETWEEN PROPOSED EATING DETECTION SYSTEM AND PREVIOUS SOLUTIONS. THREE OF THE CLASSIFICATION ALGORITHMS [4], [5], [6] WERE IMPLEMENTED OFFLINE; SINCE THESE ARE NOT EMBEDDED SOLUTIONS, THEIR POWER CONSUMPTION IS NOT REPORTED

	Window Size (s)	Accuracy	F1-Score	Precision	Recall	Power (mW)
This work	24	0.94	0.94	0.96	0.91	0.019
FitByte [38]	5	-	-	0.83	0.94	105
TinyEats [12]	4	0.95	0.95	0.95	0.95	40
Auracle [6]	3	0.91	-	0.95	0.87	OFFLINE
EarBit [4]	35	0.90	0.91	0.87	0.96	OFFLINE
AXL [5]	20	-	0.91	0.87	0.95	OFFLINE

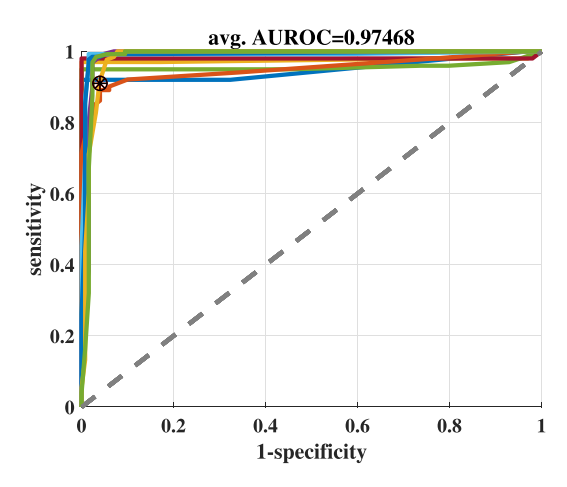


Fig. 15. Receiver operating characteristic curve (ROC) from AFUA chip measurements. These results were produced from repeated AFUA chip measurement responses to 1.6 hours of previously-unseen test data. Circuit noise produces slightly different performance from one measurement to another, with the area under ROC (AUROC) ranging from 0.95 to 0.99 (average AUROC=0.97). The highlighted point corresponds to a sensitivity of 0.91 and a specificity of 0.96.

highlighted point on the ROC is a representative operating point, where the classifier produced a sensitivity of 0.91 and a specificity of 0.96. This corresponds to a false alarm rate of (1--specificity) = 0.039.

B. System-Level Considerations

In this section, we consider the impact of using the AFUA neural network in a complete eating event detection system. To process a 500 Hz signal, the ZCR and RMS feature extraction blocks consume a total of $0.68\,\mu\mathrm{W}$ [20]. Also, the AFUA network consumes $1.1\,\mu\mathrm{W}$, assuming $I_{\mathrm{unit}}=10\,\mathrm{nA}$. Finally, a microcontroller from the MSP430x series (Texas Instruments Inc., Dallas, TX) running at $1\,\mathrm{MHz}$ consumes $180\,\mu\mathrm{W}$ when active and $0.72\,\mu\mathrm{W}$ when in standby mode [40].

The feature extraction and AFUA circuitry are always on, while the microcontroller remains in standby mode until a potential chewing event is detected. The fraction of time the microcontroller is in the active mode depends on how often the user eats, as well as the sensitivity and specificity of the AFUA network. Assuming the user spends 6% of the day eating [39], then, using the classifier operating point highlighted in Fig. 15, the fraction of time that the microcontroller is active is

ACTIVE = EAT
$$\times$$
 SENS + $(1 - \text{SPEC}) \times (1 - \text{EAT})$
= $0.06 \times 0.91 + (1 - 0.96) \times (1 - 0.06)$
= 0.09 . (20)

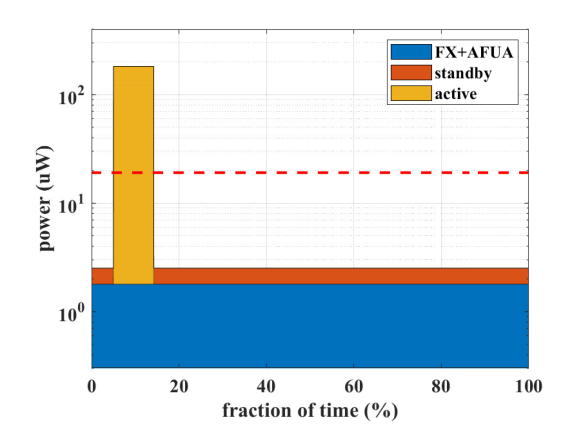


Fig. 16. Power consumption of eating detection system. The feature extraction and AFUA circuitry continuously consume $1.8\,\mu\mathrm{W}$ of power. The microcontroller is active for 9% of the time, during which it consumes $180\,\mu\mathrm{W}$ of power. For the remaining 91% of the time, the microcontoller consumes $0.72\,\mu\mathrm{W}$ while in standby mode. On average (red dashed line), the whole system consumes an estimated $18.8\,\mu\mathrm{W}$.

So, the microcontroller consumes an average of $180 \,\mu W \times 0.09 + 0.72 \,\mu W \times (1-0.09) = 16.9 \,\mu W$. As Fig. 16 shows, the average power consumption of the complete AFUA-based eating detection system is $18.8 \,\mu W$.

Table II compares our work to other recent eating detection solutions. The different approaches all yield generally the same level of classification accuracy, but our work differs in one critical aspect: while others depend on offline processing, or on tens of milliWatts of power to operate, our approach only requires an estimated $18.8 \, \mu W$.

C. Analog Versus Digital LSTM

The AFUA neural network has a total power consumption of $1.1 \,\mu\text{W}$. Unlike a digital LSTM implementation, the AFUA network is an analog circuit and does not require a front-end ADC. If we attempted to implement the system with a digital LSTM [41], [42], then it would require a 12-bit, 500 Sa/s front-end ADC [7], [43] and this ADC alone would consume over $3\,\mu\text{W}$ of power [44]. Note, the ADC would itself require an ADC driver, which typically consumes even more power than the ADC [45]; any power efficiency benefits of a digital LSTM are overwhelmed by the power demands of the ADC and ADC driver.

VII. CONCLUSION

We have introduced the AFUA—an adaptive filter unit for analog long short-term memory—as part of an eating event detection system. Measurement results of the AFUA implemented in a 0.18 μm CMOS technology showed that it can identify chewing events at a 24-second time resolution with a recall of 91% and an F1-score of 94%, while consuming 1.1 μW of power. The AFUA precludes the need for an analog-to-digital converter, and it also prevents a downstream microcontroller from unnecessarily processing irrelevant data. If a signal processing system were built around the AFUA for detecting eating episodes (that is, meals and snacks), then the whole system would consume less than $20\,\mu W$ of power. This opens up the possibility of unobtrusive, batteryless wearable devices that can be used for long-term monitoring of dietary habits.

ACKNOWLEDGMENT

The views and conclusions contained in this document are those of the authors and do not necessarily represent the official policies, either expressed or implied, of the sponsors.

REFERENCES

- K. Kang, "Nutritional counseling for obese children with obesity-related metabolic abnormalities in Korea," *Pediatr. Gastroenterol. Hepatol. Nutr.*, vol. 20, pp. 71–78, 2017.
- [2] L. O'Connor, M. Lentjes, R. Luben, K. Khaw, N. Wareham, and N. Forouhi, "Dietary dairy product intake and incident type 2 diabetes: A prospective study using dietary data from a 7-day food diary," *Diabetologia*, vol. 57, pp. 909–917, 2014.
- [3] R. Turton et al., "To go or not to go: A proof of concept study testing food-specific inhibition training for women with eating and weight disorders," Eur. Eating Disord. Rev., vol. 26, pp. 11–21, 2018.
- [4] A. Bedri et al., "EarBit: Using wearable sensors to detect eating episodes in unconstrained environments," in *Proc. ACM Interactive, Mobile, Wearable Ubiquitous Technol.*, 2017, vol. 1, pp. 1–20.
- [5] M. Farooq and E. Sazonov, "Accelerometer-based detection of food intake in free-living individuals," *IEEE Sensors J.*, vol. 18, no. 9, pp. 3752–3758, May 2018.
- [6] S. Bi et al., "Toward a wearable sensor for eating detection," in *Proc. Workshop Wearable Syst. Appl.*, 2017, pp. 17–22.
- [7] S. Bi et al., "Auracle: Detecting eating episodes with an ear-mounted sensor," Proc. ACM Interactive, Mobile, Wearable Ubiquitous Technol., 2018, vol. 2, pp. 1–27.
- [8] A. Canhoto and S. Arp, "Exploring the factors that support adoption and sustained use of health and fitness wearables," *J. Marketing Manage.*, vol. 33, pp. 32–60, 2017.
- [9] Y. Gao, H. Li, and Y. Luo, "An empirical study of wearable technology acceptance in healthcare," *Ind. Manage. Data Syst.*, vol. 115, no. 9, pp. 1704–1723, 2015.
- [10] L. Dunne et al., "The social comfort of wearable technology and gestural interaction," in *Proc. 36th Annu. Int. Conf. IEEE Eng. Med. Biol. Soc.*, 2014, pp. 4159–4162.
- [11] B. Hensel, G. Demiris, and K. Courtney, "Defining obtrusiveness in home telehealth technologies: A conceptual framework," *J. Amer. Med. Inform.*, *Assoc.*, vol. 13, pp. 428–431, 2006.
- [12] M. Nyamukuru and K. Odame, "Tiny Eats: Eating detection on a microcontroller," in *Proc. IEEE 2nd Workshop Mach. Learn. Edge Sensor Syst.*, 2020, pp. 19–23.
- [13] J. Amoh and K. Odame, "An optimized recurrent unit for ultra-low-power keyword spotting," *Proc. ACM Interactive, Mobile, Wearable Ubiquitous Technol.*, 2019, vol. 3, pp. 1–17.
- [14] I. Jordan and I. Park, "Birhythmic analog circuit maze: A nonlinear neurostimulation testbed," *Entropy*, vol. 22, 2020, Art. no. 537.
- [15] K. Adam, K. Smagulova, and A. James, "Memristive LSTM network hardware architecture for time-series predictive modeling problems," in *Proc. IEEE Asia Pacific Conf. Circuits Syst.*, 2018, pp. 459–462.
- [16] O. Krestinskaya, K. Salama, and A. James, "Learning in memristive neural network architectures using analog backpropagation circuits," *IEEE Trans. Circuits Syst. I: Regular Papers*, vol. 66, no. 2, pp. 719–732, Feb. 2019.
- [17] J. Han, H. Liu, M. Wang, Z. Li, and Y. Zhang, "ERA-LSTM: An efficient ReRAM-based architecture for long short-term memory," *IEEE Trans. Parallel Distrib. Syst.*, vol. 31, no. 6, pp. 1328–1342, Jun. 2020.

- [18] Z. Zhao, A. Srivastava, L. Peng, and Q. Chen, "Long short-term memory network design for analog computing," ACM J. Emerg. Technol. Comput. Syst., vol. 15, pp. 1–27, 2019.
- [19] Q. Li et al., "NS-FDN: Near-sensor processing architecture of feature-configurable distributed network for beyond-real-time always-on keyword spotting," *IEEE Trans. Circuits Syst. I: Regular Papers*, vol. 68, no. 5, pp. 1892–1905, May 2021.
- [20] M. Baker, S. Zhak, and R. Sarpeshkar, "A micropower envelope detector for audio applications [hearing aid applications]," in *Proc. Int. Symp. Circuits Syst.*, 2003, pp. V1–V4.
- [21] R. Sarpeshkar, M. Baker, C. Salthouse, J. Sit, L. Turicchia, and S. Zhak, "An analog bionic ear processor with zero-crossing detection," in *Proc. IEEE Int. Dig. Techn. Papers Solid-State Circuits Conf.*, 2005, pp. 78–79.
- [22] S. Hochreiter and J. Schmidhuber, "Long short-term memory," *Neural Comput.*, vol. 9, pp. 1735–1780, 1997.
 [23] K. Cho et al., "Learning phrase representations using RNN encoder-
- [23] K. Cho et al., "Learning phrase representations using RNN encoder-decoder for statistical machine translation," in *Proc. Conf. Empirical Methods Natural Lang. Process. (EMNLP)*, Oct. 2014, pp. 1724–1734.
- [24] G. Zhou, J. Wu, C. Zhang, and Z. Zhou, "Minimal gated unit for recurrent neural networks," *Int. J. Automat. Comput.*, vol. 13, pp. 226–234, 2016.
- [25] M. Ravanelli, P. Brakel, M. Omologo, and Y. Bengio, "Improving speech recognition by revising gated recurrent units," in *Proc. INTERSPEECH*, 2017, pp. 1308–1312.
- [26] M. Ravanelli and Y. Bengio, "Speaker recognition from raw waveform with sincnet," in *Proc. IEEE Spoken Lang. Technol. Workshop*, 2018, pp. 1021– 1028.
- [27] S. Strogatz, Nonlinear Dynamics and Chaos: With Applications to Physics, Biology, Chemistry, and Engineering. Boca Raton, FL, USA: CRC Press, 2018
- [28] P. Warden, "Speech commands: A dataset for limited-vocabulary speech recognition," 2018, arXiv:1804.03209.
- [29] K. Odame and M. Nyamukuru, "Analog LSTM for keyword spotting," in Proc. IEEE 4th Int. Conf. Artif. Intell. Circuits Syst., 2022, pp. 375–378.
- [30] K. Odame and B. Minch, "The translinear principle: A general framework for implementing chaotic oscillators," *Int. J. Bifurcation Chaos*, vol. 15, pp. 2559–2568, 2005.
- [31] K. Odame and B. Minch, "Implementing the Lorenz oscillator with translinear elements," *Analog Integr. Circuits Signal Process.*, vol. 59, pp. 31–41, 2009.
- [32] J. Mulder, W. Serdijn, A. Woerd, and A. V. Roermund, "Dynamic translinear RMS-DC converter," *Electron. Lett.*, vol. 32, pp. 2067–2068, 1996.
- [33] C. Enz, F. Krummenacher, and E. Vittoz, "An analytical MOS transistor model valid in all regions of operation and dedicated to low-voltage and low-current applications," *Analog Integr. Circuits Signal Process.*, vol. 8, pp. 83–114, 1995.
- [34] J. Binas, D. Neil, G. Indiveri, S. Liu, and M. Pfeiffer, "Precise deep neural network computation on imprecise low-power analog hardware," 2016, arXiv:1606.07786.
- [35] M. J. M. Pelgrom, A. C. J. Duinmaijer, and A. B. G. Welbers, "Matching properties of MOS transistors," *IEEE J. Solid-state Circuits*, vol. 24, no. 5, pp. 1433–1439, Oct. 1989.
- [36] A. Orgenci, G. Dundar, and S. Balkur, "Fault-tolerant training of neural networks in the presence of MOS transistor mismatches," *IEEE Trans. Circuits Syst. II: Analog Digit. Signal Process.*, vol. 48, no. 3, pp. 272–281, Mar. 2001.
- [37] D. Kingma and J. Ba, "Adam: A method for stochastic optimization," 2014, arXiv:1412.6980.
- [38] A. Bedri, D. Li, R. Khurana, K. Bhuwalka, and M. G. Fitbyte, "Automatic diet monitoring in unconstrained situations using multimodal sensing on eyeglasses," in *Proc. CHI Conf. Hum. Factors Comput. Syst.*, 2020, pp. 1– 12
- [39] J. Stimpson, B. Langellier, and F. Wilson, "Peer reviewed: Time spent eating, by immigrant status, race/ethnicity, and length of residence in the United States," *Preventing Chronic Dis.*, vol. 17, 2020, Art. no. 200122.
- [40] "MSP430FR596x, MSP430FR594x mixed-signal microcontrollers datasheet," Rev. G, Texas Instruments, Dallas, TX, Sep. 2020.
- [41] D. Shin, J. Lee, J. Lee, and H.-J. Yoo, "14.2 DNPU: An 8.1 TOPS/W reconfigurable CNN-RNN processor for general-purpose deep neural networks," in *Proc. IEEE Int. Solid-State Circuits Conf.*, 2017, pp. 240–241.
- [42] J. Giraldo and M. Verhelst, "Laika: A 5uW programmable LSTM accelerator for always-on keyword spotting in 65 nm CMOS," in *Proc. IEEE 44th Eur. Solid State Circuits Conf.*, 2018, pp. 166–169.
- [43] "CC2640R2F Datasheet," Rev. C, Texas Instruments, Dallas, TX, Sep. 2020.
- [44] S. Song et al., "A 769 μW battery-powered single-chip SoC with BLE for multi-modal vital sign monitoring health patches," *IEEE Trans. Biomed. Circuits Syst.*, vol. 13, no. 6, pp. 1506–1517, Dec. 2019.

[45] M. Takhti and K. A. Odame, "A power adaptive, 1.22-pW/Hz, 10-MHz read-out front-end for bio-impedance measurement," *IEEE Trans. Biomed. Circuits Syst.*, vol. 13, no. 4, pp. 725–734, Aug. 2019.



Kofi Odame (Senior Member, IEEE) is currently an Associate Professor of electrical engineering with the Thayer School of Engineering, Dartmouth College, Hanover, NH, USA. His primary research interests include analog integrated circuits for nonlinear signal processing. This work has applications in low-power electronics for implantable and wearable biomedical devices, as well as in autonomous sensor systems.



Maria Nyamukuru (Student Member, IEEE) is currently working toward the Ph.D. with the Thayer School of Engineering, Dartmouth College, Hanover, NH, USA. Her research interests include design, optimization and implementation of deep learning algorithms in resource constrained environments, with a focus on biomedical applications.



Mohsen Shahghasemi (Student Member, IEEE) received the B.Sc. degree in electronics engineering from the University of Zanjan, Zanjan, Iran, in 2010, and the M.Sc. degree in electronics engineering (microelectronics) from the Amirkabir University of Technology (Tehran Polytechnic), Tehran, Iran, in 2013. From 2017 to 2022, he was with Dartmouth College, Hanover, NH, USA, where he conducted Ph.D. research on circuit and system design for electrical impedance tomography. He is currently an Analog/Mixed-Signal Design Engineer with Apple Inc. (Cupertino, CA).



Shengjie Bi received the B.Sc. degree in electronics engineering from the University of Electronics Science and Technology of China, Chengdu, China, in 2014, and the M.Sc. degree in electrical engineering from the University of California, Los Angeles, Los Angeles, CA, USA, in 2016, and the Ph.D. degree in computer science from Dartmouth College, Hanover, NH, USA, in 2021 for work on wearable devices for automatic dietary monitoring. He is currently a Research Scientist with Meta Platforms, Inc. (Menlo Park, CA).



David Kotz (Fellow, IEEE) received the A.B. degree in computer science and physics from Dartmouth College, Hanover, NH, USA, in 1986, and the Ph.D. degree in computer science from Duke University, Durham, NC, USA, in 1991. He is currently a Provost, and a Pat and John Rosenwald Professor with the Department of Computer Science, Dartmouth College. In 2019 he was a Visiting Professor with ETH Zürich, Zürich, Switzerland, His research interests include security and privacy in smart homes, and wireless networks. He is an ACM Fellow, a 2008 Fulbright

Fellow to India, and an elected Member of Phi Beta Kappa.